

## Oxidation Behavior of Fe–25Cr–20Ni–2.8Si During Isothermal Oxidation at 1,286 K; Life-time Prediction

R. Bauer · M. Baccalaro · L. P. H. Jeurgens ·  
M. Pohl · E. J. Mittemeijer

Received: 21 August 2007 / Revised: 10 January 2008 / Published online: 16 February 2008  
© The Author(s) 2008

**Abstract** The oxidation behavior of an austenitic steel, type 1.4841, with a Cr content of 25 wt% and a high-Si content of 2.8 wt% was studied during isothermal oxidation at 1,286 K in air. A thick, crystalline Cr<sub>2</sub>O<sub>3</sub> layer, on top of a much thinner, amorphous SiO<sub>2</sub> layer, developed on the alloy substrate. After formation of a closed Cr<sub>2</sub>O<sub>3</sub> scale, parabolic growth kinetics prevailed as long as the associated constant, steady-state Cr concentration in the alloy at the substrate/oxide interface of about 13 ± 1 wt% was maintained. Upon prolonged oxidation, successive cracking and spallation of the thickening oxide scale eventually led to breakaway oxidation, because the “bulk-”Cr concentration in the interior of the alloy dropped below the critical value required to ‘heal’ the protective oxide layer after oxide spallation. Application of a lifetime prediction model of the alloy substrate under isothermal oxidation conditions allowed determination of the breakaway-oxidation time as a function of alloy-sheet thickness, by employing the Cr volume-diffusion coefficient in the alloy and the parabolic growth-rate constant, both determined in the present study by fitting calculated to experimental Cr-depletion profiles for various oxidation times.

**Keywords** Breakaway oxidation · Chemical failure · Austenitic steels · Depletion modeling · Lifetime prediction

---

R. Bauer · E. J. Mittemeijer  
Institute for Physical Metallurgy, University of Stuttgart, Stuttgart, Germany

R. Bauer · L. P. H. Jeurgens (✉) · E. J. Mittemeijer  
Max Planck Institute for Metals Research, Stuttgart, Germany  
e-mail: l.p.h.jeurgens@mf.mpg.de

M. Baccalaro  
Robert Bosch GmbH, Corporate Research/Applied Research Materials (CR/ARM),  
Stuttgart, Germany

M. Baccalaro · M. Pohl  
Ruhr-University Bochum, Institute for Materials and Materials Testing, Bochum, Germany

## Introduction

Application of austenitic, stainless-steel components in oxidizing environments at high temperatures ( $T > 1,000$  K) relies on the formation of a *protective* (i.e., thermodynamically and mechanically stable, well-adherent and slow-growing) oxide scale on the component surface. To form a protective  $\text{Cr}_2\text{O}_3$  scale on steel-component surfaces during the initial, very fast oxidation stages at high  $T$ , the nominal-Cr content in, e.g., Fe–Cr alloys, should be at least 14 wt%, depending on the oxidation temperature, the oxidizing environment and the alloy microstructure (composition, grain size, texture, surface roughness, etc.; as determined empirically in e.g., Refs. 1–3).

To sustain the external  $\text{Cr}_2\text{O}_3$  scale during prolonged operation at high  $T$ , further oxidation should proceed by the (exclusive) growth of the  $\text{Cr}_2\text{O}_3$  scale through selective oxidation of Cr from the parent alloy substrate, which is associated with a continuous depletion of Cr from the alloy substrate. Growth of the  $\text{Cr}_2\text{O}_3$  scale during prolonged oxidation is rate-limited by the diffusion of the reactants through the  $\text{Cr}_2\text{O}_3$  scale [4] (predominantly by the Cr cations, but with an increasingly important role of the oxygen anions with increasing temperature; see Refs. 5, 6 and section “Oxide-growth Kinetics”) under influence of (electro)chemical-potential gradients, and consequently, the oxide-scale-growth kinetics obeys a parabolic law. During the parabolic-growth stage, a steady-state situation occurs at the alloy/oxide interface, such that the rate of supply (i.e., flux) of Cr from the interior of the alloy towards the interface matches the rate of Cr consumption from the interface region by the growing oxide scale [4, 7, 8]. Then, as long as an infinite reservoir of Cr is available in the bulk of the alloy substrate, a constant steady-state Cr concentration is maintained at the alloy substrate at the alloy/oxide interface [4, 7, 8], which value is determined by the ratio of the parabolic growth rate constant of the oxide layer and the Cr-diffusion coefficient in the substrate and the nominal-Cr concentration in the interior of the substrate [4, 8]. Consequently, the steady-state, Cr-interface concentration is generally much higher than the equilibrium value of the Cr interface concentration for which  $\text{Cr}_2\text{O}_3$  is in local thermodynamic equilibrium with the alloy substrate at the alloy/oxide interface (*note*: this value is close to zero [9]).

However, during long-time service of a steel component of finite thickness at high temperature, the reservoir of Cr in the alloy substrate can no longer support a constant Cr concentration in the alloy substrate at the alloy/oxide interface, especially if bare, Cr-depleted alloy surface is repeatedly directly exposed to the oxidizing environment due to cracking and/or spalling of the growing-oxide scale as a result of stresses induced by e.g., growth, thermal cycling and/or mechanical abrasion. In such a case (i.e., for a finite-Cr reservoir in the substrate), the steady-state Cr concentration in the substrate at the alloy/oxide interface, as well as the ‘bulk’-Cr concentration in the interior of the substrate, start to decrease with increasing oxidation time and eventually drop below their critical concentration values required to ‘heal’ the protective  $\text{Cr}_2\text{O}_3$  scale upon (repeated) oxide-scale spallation [1–3, 9–11]. Thereby failure of the steel component is initiated. The oxidation time corresponding with the onset of such Cr-depletion-induced failure upon spalling of the oxide scale (often referred to as mechanically induced chemical

failure; cf. Ref. 10) is designated as the *breakaway oxidation time* at a certain oxidation temperature for the alloy substrate under investigation. Beyond the breakaway-oxidation time, fast oxidation of other base elements, such as Fe and Ni, from the alloy substrate occurs, associated with drastic changes in the oxide-scale morphology and the oxide-growth kinetics.

Cr<sub>2</sub>O<sub>3</sub>-scale-forming austenitic steels also contain other elements (e.g., Al or Si) at low concentrations (<2 wt%), which can form either oxide precipitates in the alloy substrate adjacent to the alloy/Cr<sub>2</sub>O<sub>3</sub> interface (“internal oxidation”) or an intermediate, thin oxide layer (of e.g., Al<sub>2</sub>O<sub>3</sub> or SiO<sub>2</sub>, respectively) between the alloy substrate and the external Cr<sub>2</sub>O<sub>3</sub> scale. Although small additions of Si to Cr<sub>2</sub>O<sub>3</sub>-scale-forming steel are known to improve its high-temperature corrosion resistance (in particular, it enhances the reformation of a protective Cr<sub>2</sub>O<sub>3</sub> scale on the bare-alloy surface after oxide spallation [3, 10, 12–15]), a fundamental understanding of this effect lacks [15–18]. The Si content corresponding with the maximum oxidation resistance (i.e., the longest breakaway oxidation time at constant temperature) appears to depend strongly on the steel microstructure [3, 10, 13, 19–22].

The present work is a study of the oxide-scale-growth kinetics, of the microstructural evolution and compositional changes, and of the breakaway-oxidation time, for the high-temperature oxidation at 1,286 K in air of a Fe–25Cr–20Ni (see section “Material and Specimen Preparation”) stainless steel with a nominal Si content of 2.8 wt%. The morphology and chemical composition of the developing oxide scale were investigated by Scanning Electron Microscopy (SEM) in combination with local Energy Dispersive X-ray analysis (EDX). The developing oxide phases were identified by X-ray Diffractometry (XRD). Auger Electron Spectroscopy (AES) was applied to establish the depth-distribution of the elements in the thin oxide scale as developed during the initial stage of fast, non-parabolic oxide growth. Further, the concentration-depth profiles of Cr and Si in the parent alloy substrate were determined for various oxidation times up to the breakaway oxidation time using Electron Probe Microanalysis (EPMA).

The experimental concentration-depth profiles were fitted to the corresponding theoretical profiles as calculated using the solute-depletion model for sheet geometries as proposed by Whittle [23]. The thus-obtained values for the parabolic growth constant of the oxide layer and the Cr-diffusion coefficient in the substrate were used to quantitatively establish the relationship between the steel-component thickness and the breakaway oxidation time under isothermal-oxidation conditions.

## Experimental Procedures

### Material and Specimen Preparation

A 500 μm-thick sheet of 1.4841 type of austenitic steel was produced (cold-rolled, annealed) in a laboratory charge by Thyssen-Krupp (Düsseldorf, Germany). The steel has the following chemical composition as determined in this study by Inductively-Coupled Plasma-Optical Emission Spectrometry (ICP-OES) [wt%]: Cr: 25.1, Ni: 20.8, Si: 2.8, Mn: 0.17, C: 0.034, S: 0.005, O: 0.012, Fe: balance. The Si-

content of 2.8 wt% is exceptionally high for a 1.4841 type of steel. The average grain size as determined by light optical microscopy of an etched cross section is  $42.6 \pm 4.2 \mu\text{m}$ . Disc-shaped specimens with a diameter of 11 mm were cut from the sheet. Next, both sides of the specimen discs were prepared by grinding with SiC-paper and subsequently polishing using diamond paste down to  $0.25 \mu\text{m}$ . After polishing the specimen discs reached a thickness of about  $300 \mu\text{m}$ . To verify the model for prediction of the breakaway-oxidation time (section “Lifetime Prediction”), one specimen was deliberately polished down to a thickness of  $140 \pm 10 \mu\text{m}$ . For experimental reasons (see section “Oxidation”) a small hole of 1.5 mm diameter was drilled close to the outer edge of each specimen. All specimens were cleaned ultrasonically in isopropanol and dried by blowing with pure compressed nitrogen gas.

After the oxidation (section “Oxidation”), alloy-substrate/oxide-layer cross sections were prepared. To this end, first a thin Au layer was sputter deposited onto the oxidized alloy-substrate surface, which served as a conducting layer for the subsequent deposition of a protective Ni capping layer by electrolytic deposition. Finally, the specimens were embedded and the cross-sections were ground and polished as described above.

## Oxidation

Oxidation experiments were performed in a conventional furnace (Heraeus M110) at 1,286 K in air. All specimens were hung in an open rack using thin wires through the hole at the specimen edge and then placed simultaneously in the furnace. For the  $300 \mu\text{m}$ -thick alloy sheets, oxidized specimens were removed from the furnace at defined time intervals of 0.17, 0.50, 1.00, 2.00, 5.53, 10.42, 25.00, 50.42, 100.25 and 216.75 h. To verify the model for prediction of the breakaway-oxidation time (section “Lifetime Prediction”), one specimen was deliberately polished down to a thickness of  $140 \pm 10 \mu\text{m}$  (section “Material and Specimen Preparation”) and oxidized for 552.00 h.

## Phase, Composition and Microstructure Analyses

XRD was employed to determine the crystalline phases in the developing oxide scale. Diffractograms were recorded in Bragg-Brentano geometry in the  $2\theta$  range of  $20^\circ$ – $130^\circ$  with a step size of  $0.1^\circ$  employing a BRUKER D500 diffractometer using Cu-K $\alpha$  radiation selected by a graphite monochromator in the diffracted beam and applying specimen rotation to improve crystal statistics. The PDF cards 52-0513 for  $\gamma$  Fe, 38-1479 for  $\text{Cr}_2\text{O}_3$  and 46-1045 for  $\text{SiO}_2$  issued by the ICDD [24] were used for phase identification.

The morphology and thickness of the oxide scale were determined with a LEO “SUPRA 35VP” SEM equipped with an Energy-Dispersive X-ray detector (EDX; OXFORD “Inca X-Sight”) for local analysis of the chemical composition.

For selected specimens corresponding with relatively short oxidation times, the element-depth distribution in the oxide scale was determined by AES sputter-depth

profiling. To this end, spectra of the Fe LMM, Ni LMM, Cr LMM, Si KLL and O KLL lines were recorded with a JEOL Jamp 7830F using a primary electron beam (field-emission cathode) of 10 keV and 15 nA (scanning an area of  $10 \times 10 \mu\text{m}^2$ ) and employing an ion-sputtering step of 30 s (focussed 3 kV  $\text{Ar}^+$  beam with a current of about  $0.7 \mu\text{A}$ , scanning an area of  $300 \times 300 \mu\text{m}^2$ ). The intensity-depth profiles of the various oxidic (i.e., from the oxide scale) and metallic (i.e., from the alloy substrate) spectral contributions were resolved from the differential AES spectra using the linear least-squares fitting procedure as implemented in the Phi-MultiPak software (version 5.0A). The sputter depth was estimated by adopting the corresponding sputter rate as determined for a well-defined reference specimen consisting of a 30 nm-thick  $\text{Ta}_2\text{O}_5$  film on Ta.

Concentration-depth profiles of Cr and Si (making point measurements with a step size of  $1 \mu\text{m}$  along a line perpendicular to both oxidized surfaces in the oxidized alloy substrate sheet) were obtained using EPMA analysis (CAMECA SX100 employing a focussed electron beam at an accelerating voltage of 15 kV and a current of 40 nA). Quantification was performed by dividing the measured Fe  $K\alpha$ , Cr  $K\alpha$ , Ni  $K\alpha$  and Si  $K\alpha$  peak intensities by the corresponding X-ray intensities recorded from standard specimens of pure Fe, Cr, Ni and Si, respectively, and employing the  $\Phi(\rho z)$  approach by Pouchou and Pichoir [25].

## Results and Discussion

### Morphology and Phase Constitution of the Grown Oxide Scale

AES analysis of the specimen surface prior to oxidation showed that the native oxide on the as-prepared alloy substrate surface consists of a  $\sim 20$ – $30$  nm-thick oxide scale predominantly composed of Cr-oxide with some mixed (Mn, Fe, Ni)-oxides (i.e., an oxide solid solution, a spinel and/or a doped oxide phase). Moreover, the AES sputter-depth analysis of an as-prepared specimen showed the presence of some  $\text{SiO}_2$  at the interface between the parent alloy substrate and the native oxide.

An AES sputter-depth profile as recorded from the alloy after 30 min of oxidation at 1,286 K is shown in Fig. 1. It follows that a double-layered oxide structure has developed, which consists of a *bottom* layer of  $\text{SiO}_2$  adjacent to the alloy/oxide interface and a *top* layer consisting of predominantly  $\text{Cr}_2\text{O}_3$  with some mixed (Ni,Cr,Fe)-oxides and/or  $\text{NiCr}_2\text{O}_4$  spinel oxides close to the outer oxide surface.

The XRD analyses (e.g., see Fig. 2) showed that the oxide scales are indeed mainly constituted of  $\text{Cr}_2\text{O}_3$  and some small amounts of mixed oxides of the type (Cr,Fe,Mn) $_3\text{O}_4$ . No peaks due to  $\text{SiO}_2$  appear in the recorded diffractograms after prolonged oxidation times, although the  $\text{SiO}_2$  layer thickness is about  $0.37 \pm 0.06 \mu\text{m}$  after oxidation for 216.75 h and the typical austenite reflections pertaining to the alloy substrate always show up in the diffractograms (i.e., the XRD-information depth exceeds the thickness of the entire oxide scale). The XRD detection limit for a single-phase layer is about 100 nm. Hence, it is concluded that the  $\text{SiO}_2$  bottom layer (cf. the AES results discussed above) is fully amorphous (in accordance with results reported in Ref. 22).

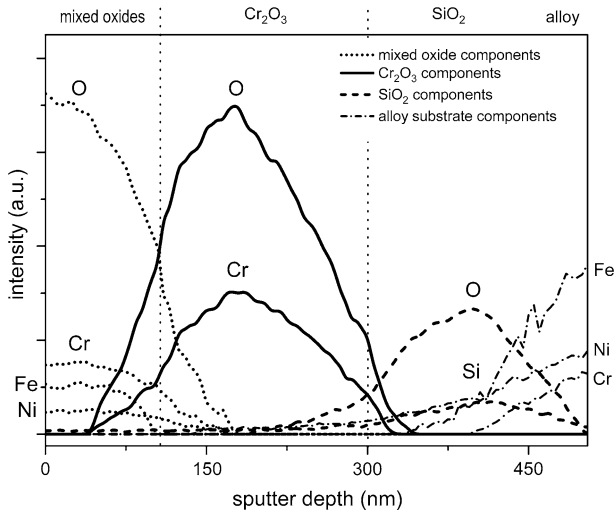


**Fig. 1** Intensity-depth profile of the resolved elemental species in the oxide scale and the parent alloy (300  $\mu\text{m}$  thick) after 30 min of oxidation at 1,286 K as obtained by AES sputter-depth profiling. The different spectral components, as obtained from the measured O KLL, Si KLL, Cr LMM, Fe LMM and Ni LMM Auger spectra by LSS fitting (section “Phase, Composition and Microstructure Analyses”), are associated either with the oxide surface (designated as ‘mixed-oxide’ region), or the Cr<sub>2</sub>O<sub>3</sub> top layer, or the SiO<sub>2</sub> bottom layer, or the parent alloy

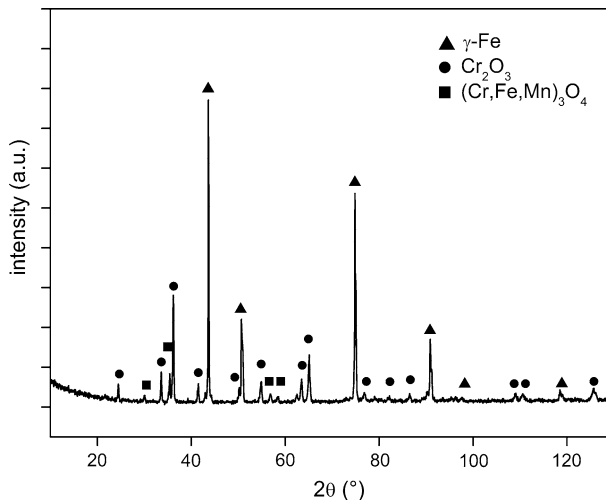


**Fig. 2** X-ray diffractogram (Cu K $\alpha$  radiation) of the oxidized alloy (300  $\mu\text{m}$  thick) after 216.75 h of oxidation at 1,286 K. Some reflections of very low intensity could not be identified and are most probably associated with mixed oxides at the oxide surface

The development of a double-layered oxide structure is confirmed by cross-sectional SEM (and local EDX) analysis (Fig. 3). After 1 h of oxidation at 1,286 K, a closed Cr<sub>2</sub>O<sub>3</sub> top layer in combination with a much thinner (possibly not yet fully

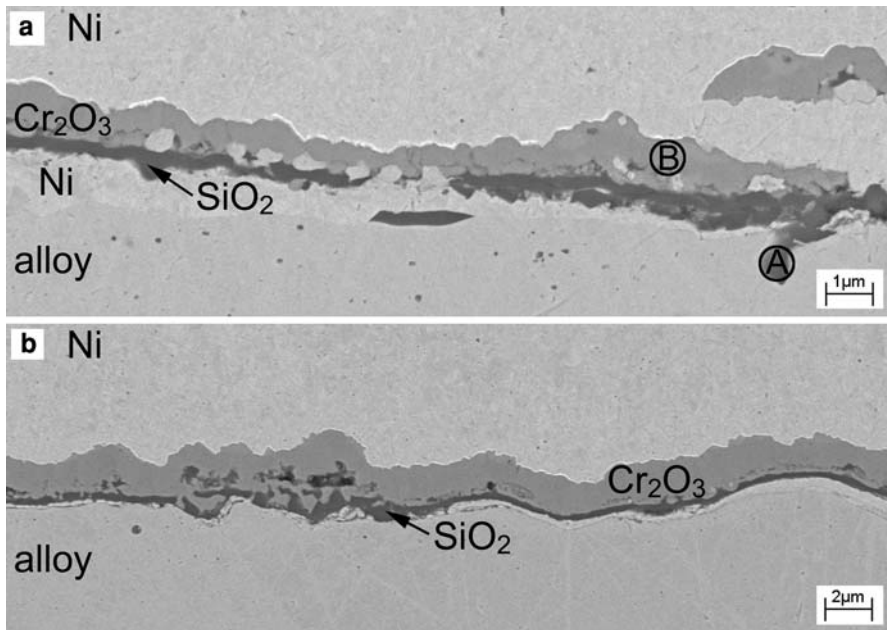


**Fig. 3** Scanning-electron micrographs of cross sections of the oxidized alloy (300  $\mu\text{m}$  thick) after (a) 1 h and (b) 5.53 h of oxidation at 1,286 K. EDX analysis (in wt%) in (a) was performed at the indicated positions A (C: 15, Si: 20, O: 65) and B (C: 2, Cr: 58, Fe: 1, O: 39). The Ni between the oxide scale and the original alloy/oxide interface originates from the metallographic preparation of the cross-sections (section “Material and Specimen Preparation”)

closed)  $\text{SiO}_2$  bottom layer has developed on the alloy surface (Fig. 3a). Protrusions (i.e., pegs) of  $\text{SiO}_2$  and  $\text{Cr}_2\text{O}_3$  occur along grain boundaries of the substrate which intersect the alloy/oxide interface. Apparently, these pegs are formed by internal oxidation along alloy grain boundaries during the initial-oxidation stage (i.e., up to the stage where a closed  $\text{Cr}_2\text{O}_3$  scale has formed), because the alloy grain boundaries provide fast-diffusion paths for both outward diffusion (surface segregation) of Si and Cr and inward diffusion of O (similar to the formation of Y-oxide pegs in MCrAlY coating systems as discussed in Ref. 26). Upon further oxidation, the initially grown  $\text{SiO}_2$  and  $\text{Cr}_2\text{O}_3$  oxide pegs become gradually incorporated in the thickening oxide scale, resulting in more uniform  $\text{Cr}_2\text{O}_3$  and  $\text{SiO}_2$  layer thicknesses for increasing oxidation times. The eventual occurrence of a relatively thick, closed  $\text{Cr}_2\text{O}_3$  scale adjacent to the surface and a much thinner, but also closed,  $\text{SiO}_2$  bottom layer adjacent to the substrate is shown by cross-sectional SEM analysis after 5.53 h of oxidation (Fig. 3b).

The oxide scale after more prolonged oxidation experienced a high degree of spallation upon cooling to room temperature, which hindered the preparation of the alloy/oxide cross-sections for metallographic investigations (e.g., often a Ni layer originating from the electrolytic deposition preparation step (section “Material and Specimen Preparation”) was found in-between the  $\text{Cr}_2\text{O}_3$  scale and the  $\text{SiO}_2$  layer; see Fig. 3). An enhanced degree of oxide-scale spallation for Si-containing

austenitic steels was reported in Refs. 12, 14, 15, 27 and ascribed to the presence of a thin  $\text{SiO}_2$  layer at the alloy/oxide interface. The effect could be due to the much lower linear thermal-expansion coefficient,  $\alpha$ , of  $\text{SiO}_2$  ( $\alpha \sim 0.5 \times 10^{-6} \text{ K}^{-1}$ ) as compared to those of  $\text{Cr}_2\text{O}_3$  ( $\alpha \sim 8.5 \times 10^{-6} \text{ K}^{-1}$ ) and the parent alloy ( $\alpha \sim 17.8 \times 10^{-6} \text{ K}^{-1}$ ) [28]. Hence, it can be expected that high thermal, compressive stresses build up in the  $\text{SiO}_2$  layer at the alloy/oxide interface upon cooling. Oxide spallation occurred in particular at the alloy-substrate/ $\text{SiO}_2$ -scale interface (Fig. 4a), but also across the  $\text{SiO}_2$ -scale and at the  $\text{SiO}_2$ -scale/ $\text{Cr}_2\text{O}_3$ -scale interface (marked area in Fig. 4a). Preferred oxide-scale spallation along the alloy-substrate/ $\text{SiO}_2$ -scale interface may be expected from the difference in thermal expansion coefficient between  $\text{SiO}_2$  and the alloy being larger than the corresponding difference between  $\text{SiO}_2$  and  $\text{Cr}_2\text{O}_3$  (see also Ref. 22). Additionally, a significant weakening of the alloy/ $\text{SiO}_2$  interface is expected to occur when

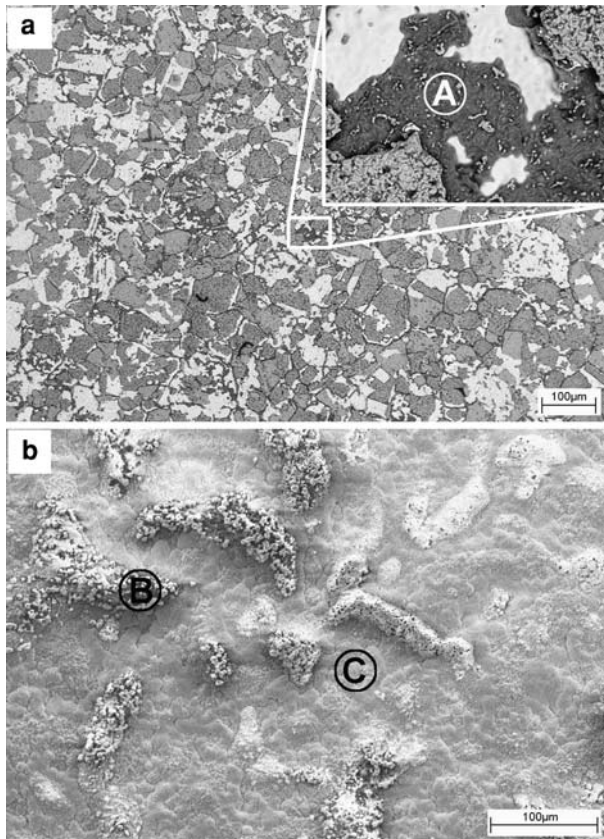


**Fig. 4** Scanning-electron micrographs of the oxidized alloy surface after (a) 2 h (300  $\mu\text{m}$  thick) and (b) 552 h (140  $\mu\text{m}$  thick) of oxidation (breakaway stage) at 1,286 K. The inset of (a) shows a magnification of the exposed surface after spallation of the oxide scale along the  $\text{Cr}_2\text{O}_3/\text{SiO}_2$ -interface. EDX analyses (in wt%) were performed at the indicated positions A (C: 4, Si: 40, O: 56), B (Si: 3, Mn: 12, Cr: 54, Fe: 1, Ni: 2, O: 28) and C (Mn: 5, Cr: 53, Fe: 2, Ni: 1, O: 39)



impurities such as S and C, originating from the alloy interior, segregate at the alloy/SiO<sub>2</sub> interface (e.g., Ref. 20). Indeed, AES analysis performed in this study of the exposed alloy surface after oxide spallation, in some cases indicated the presence of small amounts of S at the fractured alloy-substrate surface (even although the S impurity content of the alloy is as low as 0.005 wt%; see section “Material and Specimen Preparation”).

After about 100 h of isothermal oxidation at 1,286 K (i.e., already prior to breakaway oxidation), cross-sectional SEM analysis and local EDX analysis reveal the formation of pegs and internal precipitates of SiO<sub>2</sub>, Cr<sub>2</sub>O<sub>3</sub> and Cr<sub>2</sub>N (see section “Phase, Composition and Microstructure Analyses”) along the grain boundaries in the alloy, as well as the formation of plate-like Cr<sub>2</sub>N precipitates within the grains (cf. Fig. 5 for a cross-sectional SEM micrograph after 216.75 h) (see Ref. 29). This suggests that O<sub>2</sub> gas and N<sub>2</sub> gas from the oxidizing environment have come in direct contact with patches of bare alloy surface and O and N have subsequently diffused (along alloy-substrate grain boundaries) to react with either Si or Cr in less-depleted regions in the interior of the alloy substrate. This implies that extensive cracking and/or spallation of the oxide scale not only occurs upon cooling, but in particular also during isothermal oxidation (at 1,286 K) beyond a certain critical thickness, due to the continuous built-up of growth stresses (compressive) in the oxide scale. Since interstitial diffusion of nitrogen in the bulk alloy is relatively fast, Cr<sub>2</sub>N needs not only precipitate at grain boundaries (round particles), but can also precipitate within the grains (plate-like and/or needle-shaped precipitates).

If the steady-state-Cr concentration at the alloy/oxide interface is lower than (or has dropped below) the critical value required to reform a protective (i.e., closed and parabolically-growing) Cr<sub>2</sub>O<sub>3</sub> scale on the exposed part of the alloy surface after cracking and/or spalling of the oxide scale (sections “Introduction” and “Compositional Changes in the Alloy Substrate”), an Fe-rich Cr-oxide pit may develop, penetrating into the alloy substrate until the Cr concentration in the alloy substrate adjacent to the base of the oxide pit has risen to a value sufficiently large to allow formation of a closed Cr<sub>2</sub>O<sub>3</sub> ‘healing’ layer at the base of the oxide pit (thereby

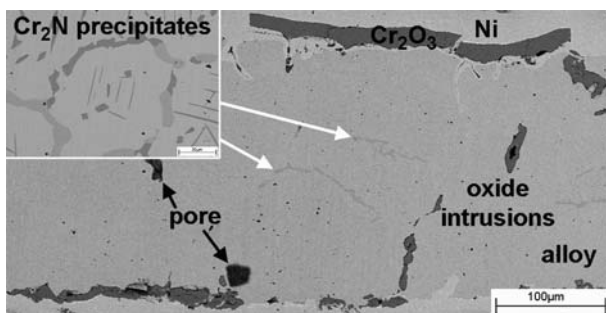


**Fig. 5** Scanning-electron micrograph of a cross section of the oxidized alloy (300 μm thick) after 216.75 h oxidation at 1,286 K. Internal oxidation and precipitation of Cr<sub>2</sub>N has already occurred long before breakaway oxidation due to fracturing and/or spallation of the growing oxide scale during isothermal oxidation. The inset shows a magnification of Cr<sub>2</sub>N precipitates (EDX (in wt%): C: 6, N: 12, Cr: 77, Fe: 5) developed along grain boundaries in the substrate and inside the substrate grains

effectively ‘healing’ the protective  $\text{Cr}_2\text{O}_3$  layer) [2, 3]. This explains the formation of inner oxides and nitrides already (long) before breakaway oxidation, but growth of such oxides and nitrides is halted as soon as the protective  $\text{Cr}_2\text{O}_3$  scale has been locally ‘healed’. Eventually, the Cr concentration in the interior of the alloy substrate decreases below the critical-healing concentration (i.e., to stop the inward-penetrating oxide pit after oxide spallation; see above). Then breakaway oxidation will occur upon renewed oxide spallation, as indicated by a drastic change in oxide-surface morphology due to the formation and rapid growth of porous (Mn,Fe,Ni)-rich oxide phases on the specimen surface; see the SEM and EDX analysis of an 140  $\mu\text{m}$ -thick alloy sheet after 552 h of oxidation at 1,286 K within the breakaway oxidation stage (Fig. 4b). For the oxidation of the 300  $\mu\text{m}$ -thick alloy sheets at 1,286 K (see sections “Material and Specimen Preparation” and “Oxidation”), the stage of breakaway oxidation was never reached for the longest oxidation time of 216.75 h studied.

### Oxide-growth Kinetics

The average thickness of the  $\text{Cr}_2\text{O}_3$  top and  $\text{SiO}_2$  bottom layer has been determined as function of oxidation time by cross-sectional SEM analysis (section “Phase, Composition and Microstructure Analyses”). Except for the very initial stages of oxidation (then a closed  $\text{Cr}_2\text{O}_3$  layer has not yet developed; see section “Morphology and Phase Constitution of the Grown Oxide Scale”), the oxide-layer growth kinetics of the  $\text{Cr}_2\text{O}_3$  layer follow a parabolic growth law with a rate constant of  $k_{\text{Cr}_2\text{O}_3} = 2.4(\pm 1.1) \times 10^{-16} \text{ m}^2/\text{s}$  before breakaway oxidation (Fig. 6a). The obtained  $k_{\text{Cr}_2\text{O}_3}$  value for  $\text{Cr}_2\text{O}_3$  is in good agreement with a corresponding value of  $2.0 \times 10^{-16} \text{ m}^2/\text{s}$  reported in Ref. 9.

Due to the pronounced formation of  $\text{SiO}_2$  pegs along alloy-substrate grain boundaries, which intersect the alloy-substrate/oxide-layer interface (section “Morphology and Phase Constitution of the Grown Oxide Scale”), the corresponding  $\text{SiO}_2$ -layer thickness values, as determined by cross-sectional SEM, exhibit a relatively large scatter, especially for shorter oxidation times (Fig. 6b). Adopting parabolic-growth kinetics, yet, an approximate value of  $1.1(\pm 0.7) \times 10^{-19} \text{ m}^2/\text{s}$  for the  $\text{SiO}_2$  parabolic growth-rate constant has been obtained; this value is an order of magnitude lower than the corresponding values, in the range of  $1 \times 10^{-18}$  to  $2 \times 10^{-18} \text{ m}^2/\text{s}$ , determined for the high-temperature oxidation of pure Si [30] (i.e., in the absence of a  $\text{Cr}_2\text{O}_3$  top layer), but it is of the same order of magnitude as the corresponding values, in the range of  $0.52 \times 10^{-19}$  to  $4.4 \times 10^{-19} \text{ m}^2/\text{s}$ , reported for the oxidation of a Fe–20Cr–25Ni steel with a very low Si content, in the range of 0.45–0.75 wt%, in the temperature range of 1,173–1,203 K [10]. It follows that the parabolic growth-rate constant of the  $\text{SiO}_2$  bottom layer ( $k_{\text{SiO}_2} = 1.1(\pm 0.7) \times 10^{-19} \text{ m}^2/\text{s}$ ) at 1,286 K is about three orders of magnitude smaller than that of the  $\text{Cr}_2\text{O}_3$  top layer ( $k_{\text{Cr}_2\text{O}_3} = 2.4(\pm 1.1) \times 10^{-16} \text{ m}^2/\text{s}$ ).

It has been often stated, that, in the absence of a bottom  $\text{SiO}_2$  layer, the oxide-growth rate for a closed oxide layer in the parabolic-growth regime is limited by outward diffusion of Cr cations through the  $\text{Cr}_2\text{O}_3$  scale [5, 6]. The  $\text{SiO}_2$  bottom

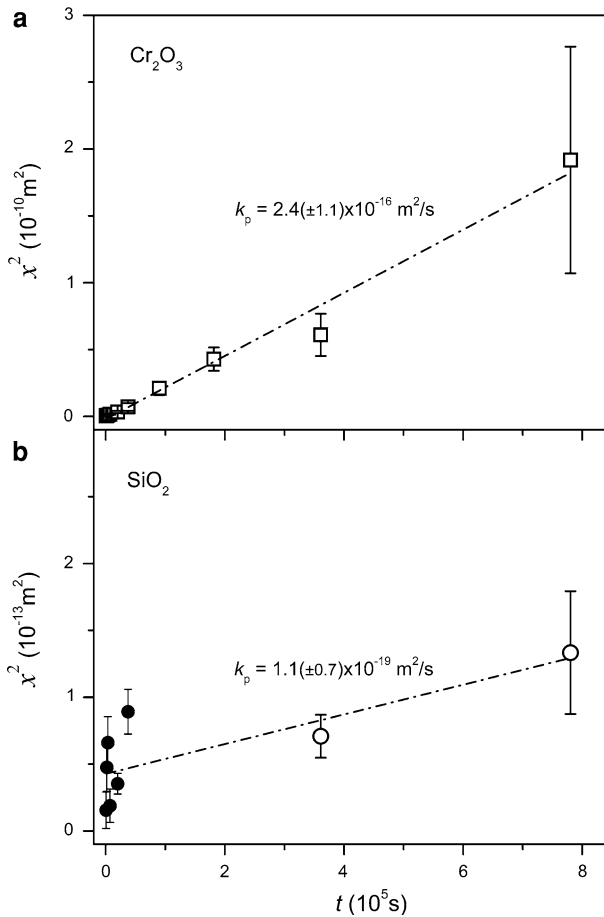


**Fig. 6** Plots of the squared oxide-layer thickness,  $x$ , for the (a)  $\text{Cr}_2\text{O}_3$  and (b)  $\text{SiO}_2$  sublayers versus the oxidation time,  $t$ , for the oxidation of the alloy (300  $\mu\text{m}$  thick) at 1,286 K in air. The data points ‘■/•’ are used to indicate that the oxide layers have not been fully closed yet; the open markers pertain to a closed oxide layer. The dash-dotted lines represent linear fits through the (open and solid) data points according to the parabolic growth law,  $x^2 = k \cdot t + x_0$ , where  $x_0$  is a constant expressing the possible occurrence of a transient (non-parabolic) growth stage

layer might act as an additional diffusion barrier for Cr-cation outward diffusion, in particular recognizing the absence of grain boundaries in the amorphous  $\text{SiO}_2$  layer [15, 20, 21]. It follows that then the effective parabolic-growth-rate constant for the  $\text{Cr}_2\text{O}_3$  layer should be lower in the presence of a  $\text{SiO}_2$  bottom layer.

#### Compositional Changes in the Alloy Substrate

The Cr and Si concentration-depth profiles as determined by EPMA line-scan analyses of oxidized specimen cross sections for oxidation times from 10 min to

216.75 h (section “Phase, Composition and Microstructure Analyses”) at the oxidation temperature of 1,286 K are shown in Fig. 7a and b, respectively. It follows that the Cr concentration in the alloy at the alloy/oxide interface decreases with increasing oxidation time towards an approximately constant value of about  $13(\pm 1)$  wt% (see Fig. 8a), reached during the parabolic oxide-growth stage (which starts after approximately 5–10.4 h of oxidation). Unfortunately, the rough interface between the oxide scale and the alloy (section “Morphology and Phase Constitution of the Grown Oxide Scale”) in combination with the limited lateral resolution of EPMA hinders an accurate determination of the Cr concentration specifically at the alloy/oxide interface,<sup>1</sup> especially for the steep Cr-depletion profiles developing in the alloy at short oxidation times. Also, in some cases distinct differences were found between the Cr-depletion profiles as measured at the opposite sides of the specimen sheet, in particular for long oxidation times (cf. Cr-concentration profiles after 100 h and 216.75 h in Fig. 7a). This is attributed mainly to local differences in the degree of cracking and/or spallation of the oxide scale during prolonged isothermal oxidation at 1,286 K (section “Morphology and Phase Constitution of the Grown Oxide Scale”); local inhomogeneities of the alloy microstructure (in particular, the Si content and alloy grain size) might also play a role here).

The Si concentration in the alloy substrate at the alloy/oxide interface initially decreases with increasing oxidation time from its bulk value of 2.8 wt% to a value in the range of 2.4–2.7 wt% (Fig. 7b). However, from the onset of the parabolic-oxide-growth stage (i.e., after approximately 5–10.4 h of oxidation), the Si-interface concentration increases with increasing oxidation time and eventually, after about 33 h of oxidation, becomes slightly larger than the bulk value (Fig. 8b). Apparently, Si depletion only occurs until a continuously closed SiO<sub>2</sub> bottom layer has formed, i.e., until about 5–10.4 h of oxidation. The subsequent enrichment of Si in the substrate at the alloy/oxide interface is attributed to one or a combination of the following factors.

- (i) After the formation of a closed SiO<sub>2</sub> layer, the rate of segregation of Si from the interior of the alloy towards the alloy/oxide interface exceeds the rate of incorporation of Si from the alloy into the growing SiO<sub>2</sub> layer (cf. Ref. 10).
- (ii) Since the growth of the SiO<sub>2</sub> layer is slower than that of the corresponding Cr<sub>2</sub>O<sub>3</sub> layer (section “Oxide-Growth Kinetics”), the Cr depletion in the alloy substrate will be more pronounced than the Si depletion in the substrate, resulting in an effective increase of the Si/Cr atomic ratio and thereby an (only) relative enrichment of Si in the substrate at the alloy/oxide interface occurs.
- (iii) The amount of Si incorporated by the growing SiO<sub>2</sub> layer is smaller than the amount of Si that piles up at the alloy/oxide interface as a consequence of the

<sup>1</sup> The lateral resolution of the EPMA is about  $\sim 1.5$   $\mu\text{m}$ , which is much lower than the corresponding spatial resolution of the order of 10 nm as holds for AES cross-sectional line-scan analysis. Consequently, for the Cr-depletion profiles with relatively large concentration gradients, developing during the initial oxide-growth stage (see Fig. 7a), the estimated accuracy in the determination of the composition in the substrate at the alloy/oxide interface by EPMA is about 1–2 wt%, [31].

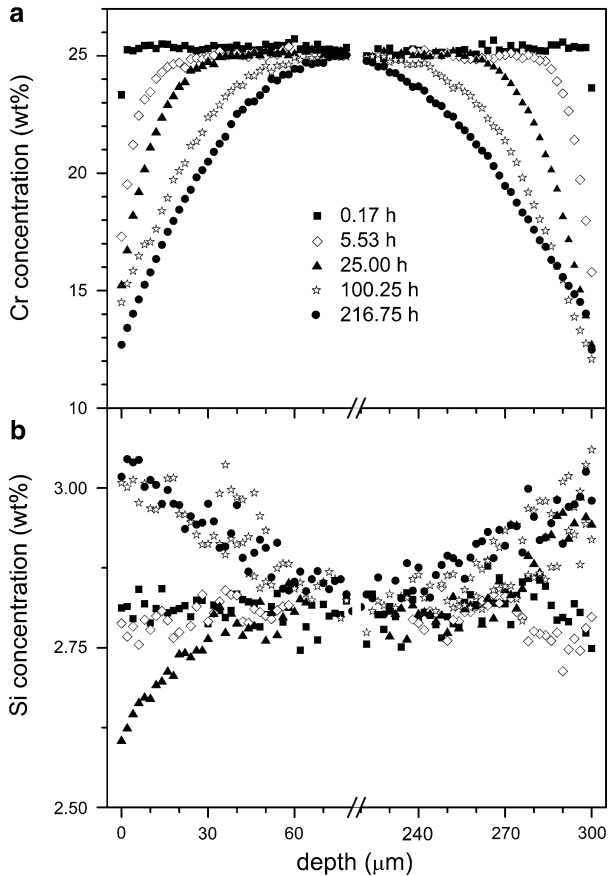


**Fig. 7** Concentration-depth profiles (in wt%) of (a) Cr and (b) Si in the oxidized alloy (300  $\mu\text{m}$  thick) after oxidation at 1,286 K for various selected oxidation times up to 216.75 h, as measured by EPMA on alloy/oxide cross-sections along lines perpendicular to the oxidized specimen surfaces (section “Phase, Composition and Microstructure Analyses”). *Note:* only a representative selection of all measured concentration-depth profiles and measured points are shown here for clarity

oxidation-induced recession of the alloy/oxide interface into the substrate and too slow diffusion of Si in the alloy to level off the Si concentration gradient; cf. Ref. 7.

A measured Cr-depletion profile for the oxidized specimen with an original nominal sheet thickness of about  $140 \pm 10 \mu\text{m}$  (see section “Oxidation”) after 552 h of oxidation at 1,286 K, i.e., after entering the *breakaway oxidation* stage, is shown in Fig. 9. The spikes in the Cr concentration in the interior of the alloy substrate correspond with internal  $\text{Cr}_2\text{O}_3$  and/or  $\text{Cr}_2\text{N}$  precipitates formed upon cracking and/or spalling of the oxide scale upon continued oxidation during the breakaway-oxidation stage (as also observed to a lesser extent already prior to the breakaway-oxidation stage for the oxidation of 300  $\mu\text{m}$ -thick alloy sheets upon spallation and

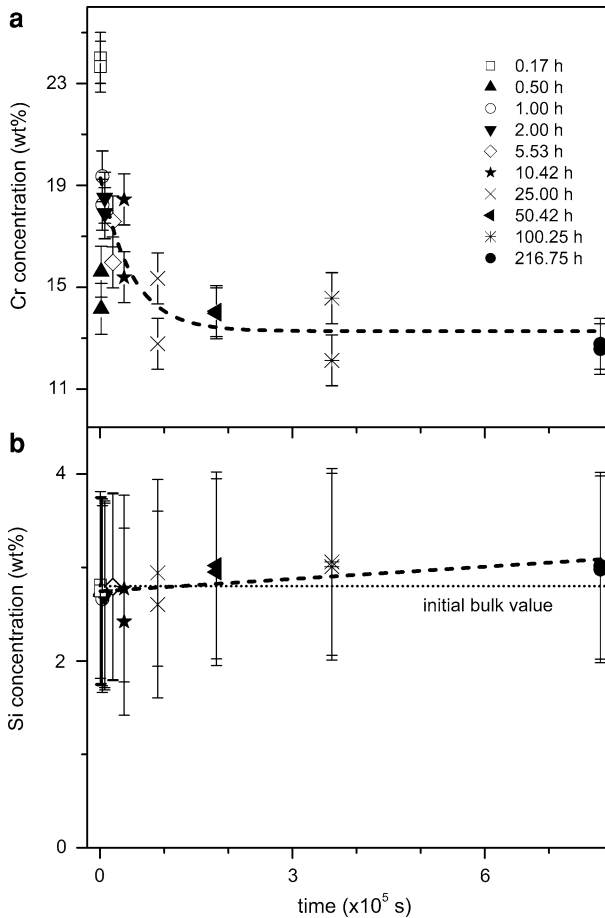


**Fig. 8** Interface concentration (in wt%) of (a) Cr and (b) Si in the alloy (300  $\mu\text{m}$  thick) substrate adjacent to the alloy/oxide interface as a function of the oxidation time, as measured by EPMA after oxidation at 1,286 K. See also Fig. 7

subsequent healing of the oxide scale; see section “Morphology and Phase Constitution of the Grown Oxide Scale”). Clearly, the Cr-depletion profiles from opposite sides of the sheet have “overlapped” and, consequently, the *midsection* Cr concentration in the interior of the sheet has dropped below its initial bulk value of 25 wt%; i.e., the Cr concentration in the *midsection* of the  $140 \pm 10$   $\mu\text{m}$  thick alloy sheet after 552 h of oxidation at 1,286 K is only about  $11.6 \pm 1$  wt% (Fig. 9). Once the *midsection* Cr concentration in the interior of the specimen has dropped below its initial bulk value, a constant Cr concentration in the alloy at the alloy/oxide interface of  $13(\pm 1)$  wt% (as reached during the parabolic growth regime; see above and Fig. 8a) can no longer be maintained; indeed, the Cr-interface concentration of the  $140 \pm 10$   $\mu\text{m}$ -thick alloy sheet after 552 h of oxidation at 1,286 K is only about  $8.9 \pm 1$  wt% (Fig. 9). The corresponding Si-concentration-depth profile after reaching breakaway oxidation is more or less flat (i.e., the slight Si enrichment as

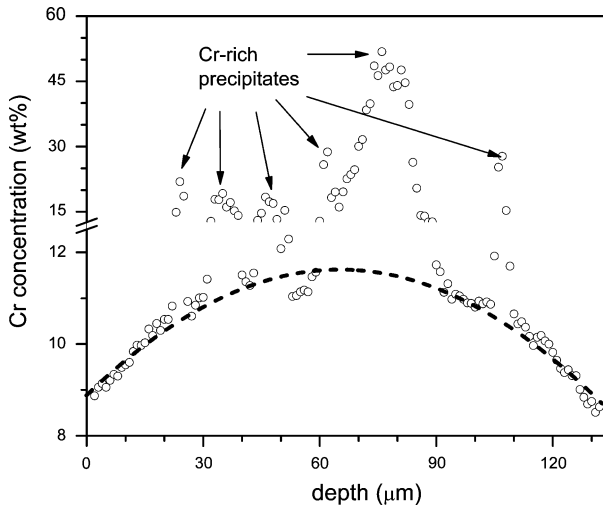


**Fig. 9** Concentration-depth profile of Cr in the oxidized alloy (140  $\mu\text{m}$  thick) after oxidation at 1,286 K for 552 h, as measured by EPMA. The spikes in the Cr concentration at certain depths below the specimen surface correspond with the location of internal precipitates of Cr-oxide and Cr-nitride (cf. Fig. 5)

observed during the parabolic-growth stage has disappeared; see above) with an average Si concentration in the range of 2.5–2.7 wt% (i.e., only slightly lower than the initial, Si-bulk concentration of 2.8 wt%).

### Lifetime Prediction

As discussed in sections “Introduction” and “Morphology and Phase Constitution of the Grown Oxide Scale”, after prolonged oxidation the reservoir of Cr in the alloy substrate can no longer sustain a constant, steady-state Cr-interface concentration. At this stage, both the Cr-interface concentration,  $C_{\text{Cr}}^{\text{interf}}$ , and the ‘bulk’-Cr concentration in the interior of the alloy-substrate,  $C_{\text{Cr}}^{\text{centre}}$ , start to decrease with increasing oxidation time. Eventually,  $C_{\text{Cr}}^{\text{centre}}$  drops below the critical-healing concentration  ${}^*C_{\text{Cr}}$ , which is required to ‘heal’ the protective  $\text{Cr}_2\text{O}_3$  layer after oxide spallation (i.e., to stop the inwardly penetrating oxide pit after oxide spallation; see section “Morphology and Phase Constitution of the Grown Oxide Scale”) [1–3, 7, 10, 11, 32]. Then breakaway oxidation occurs. An experimentally observed value of  ${}^*C_{\text{Cr}}$  for the high-temperature oxidation of an austenitic steel with composition similar to that of the studied Fe–25Cr–20Ni–2.8Si alloy within the oxidation temperature range of 1,023–1,373 K is 16 wt% [3]. This value of  ${}^*C_{\text{Cr}}$  refers to the Cr concentration in the alloy immediately below oxide pits, which have penetrated into the alloy substrate upon spalling of the initial, protective- $\text{Cr}_2\text{O}_3$  layer and which just have been halted by the formation of a closed  $\text{Cr}_2\text{O}_3$  layer at their base (see Ref. 3 and discussion in section “Morphology and Phase Constitution of the Grown Oxide Scale”). Note that this empirical value of  ${}^*C_{\text{Cr}}$  is larger than the steady-state-Cr concentration at the

alloy/oxide interface (as established during the parabolic-growth stage), which implies that pit formation up to a certain depth will always occur upon oxide spallation (i.e., also before breakaway oxidation).

A lifetime prediction of Fe–25Cr–20Ni–2.8Si sheets under isothermal oxidation conditions, i.e. the breakaway oxidation time, can now be assessed by the time for which the midsection Cr concentration in the interior of the specimen drops below the critical-healing concentration of  ${}^*C_{\text{Cr}} = 16 \text{ wt}\%$  [3, 9]. On the basis of an appropriate diffusion model (see below) the breakaway-oxidation time can then be calculated as a function of the sheet thickness.

The Cr-depletion profile developing in austenitic steels upon isothermal oxidation in the parabolic oxide-layer-growth regime can be evaluated adopting a theoretical treatment by Whittle [23]. Provided that parabolic oxide-layer-growth kinetics prevail (here the oxide growth is determined by transport within the  $\text{Cr}_2\text{O}_3$  scale) and neglecting both the oxidation-induced recession of the alloy/oxide interface into the substrate and a concentration dependence of the chemical-diffusion coefficient of Cr in the substrate alloy, an analytical expression can be derived for the Cr-depletion profile in the substrate as a function of the oxidation time at constant temperature, according to [10, 23]

$$C_{\text{Cr,exp}}(t, z) = C_{\text{Cr}}^{\text{centre}} - \frac{100 \cdot M_{\text{Cr}}}{M_{\text{alloy}}} \frac{1}{2 \cdot \text{PBR}} \left( \frac{\pi \cdot k_{\text{Cr}_2\text{O}_3}}{D_{\text{Cr}}} \right)^{1/2} \sum_{n=0}^{\infty} \left( \text{erfc} \left[ \frac{2 \cdot n \cdot w + z}{2(D_{\text{Cr}} \cdot t)^{1/2}} \right] + \dots \right. \\ \left. \dots + \text{erfc} \left[ \frac{2 \cdot (n+1) \cdot w - z}{2(D_{\text{Cr}} \cdot t)^{1/2}} \right] \right) \quad (1)$$

where  $C_{\text{Cr,exp}}(t, z)$  [wt%] is the measured Cr concentration at depth  $z$  [m] below the oxide/alloy interface at time  $t$  [s];  $M_{\text{Cr}}$  and  $M_{\text{alloy}}$  [ $\text{g mol}^{-1}$ ] are the atomic weights of Cr metal ( $52.00 \text{ g mol}^{-1}$ ) and the alloy (*here*:  $54.68 \text{ g mol}^{-1}$ ), respectively;  $w$  [m] corresponds to one half of the sample sheet thickness; PBR is the Pilling–Bedworth Ratio (i.e., 2.10 for  $\text{Cr}_2\text{O}_3$ , 2.15 for  $\text{SiO}_2$ );  $k_{\text{Cr}_2\text{O}_3}$  ( $\text{m}^2 \text{ s}^{-1}$ ) is the parabolic-growth-rate constant of the  $\text{Cr}_2\text{O}_3$  scale; and  $D_{\text{Cr}}$  ( $\text{m}^2 \text{ s}^{-1}$ ) is the chemical-diffusion coefficient of Cr.

Application of this model requires that the chemical-diffusion coefficient of Cr in the alloy and the parabolic growth rate constant of the developing  $\text{Cr}_2\text{O}_3$  scale are known for the specific alloy and oxidation conditions considered. A set of values of  $k_{\text{Cr}_2\text{O}_3}^i$  and  $D_{\text{Cr}}^i$  for each  $i$ th Cr-depletion profile have been determined by fitting of calculated Cr-concentration depth profiles to the corresponding experimental ones, as measured for oxidation times between 5.53 and 100.25 h. To account for the experimental uncertainty in the position of the alloy/oxide interface (section “Compositional Changes in the Alloy Substrate”), the alloy/oxide interface position was adopted as a fit variable for each depth profile as well. In particular the experimentally determined, Cr-depletion profiles for oxidation times between 5.53 and 100.25 h at 1,286 K (as obtained for opposite sides of the alloy sheet) were fitted, because for this oxidation time range and temperature a closed  $\text{Cr}_2\text{O}_3$  layer



occurs and parabolic-oxide growth prevails (sections “Morphology and Phase Constitution of the Grown Oxide Scale” and “Oxide-Growth Kinetics”; extensive spalling of the oxide scale takes place for oxidation times beyond 100.25 h). Validity of the model requires that all fitted Cr-depletion profiles (as measured for different oxidation times) can be described well with the same optimized values of the parabolic-growth-rate constant and the Cr-diffusion coefficient (resulting in the same (calculated) value for the constant steady-state-Cr concentration in the substrate at the alloy/oxide interface; section “Introduction”). In practice, local differences in e.g., alloy microstructure, degree of oxide spallation and oxide morphology (e.g., locally varying thickness of the  $\text{Cr}_2\text{O}_3$  and  $\text{SiO}_2$  layers) cause local differences of, in particular, the governing parabolic oxide growth rate (note the differences in the Cr-depletion profiles pertaining to opposite sides of an oxidized alloy sheet for the same oxidation time; see section “Compositional Changes in the Alloy Substrate”). To ensure that the fitting procedure strives for similar values of the fitted Cr-diffusion coefficient and the calculated steady-state, Cr-interface concentration for each fitted Cr-depletion profile, all Cr-depletion profiles were simultaneously fitted (i.e., in a single run using the Nelder–Mead simplex method as implemented in Matlab [33]) by minimization of the following mean-squared error (MSE)

$$\text{MSE} = \sum_{i=n}^N \left[ \left( \frac{{}^i C_{\text{Cr,calc}} - {}^i C_{\text{Cr,exp}}}{{}^i C_{\text{Cr,exp}}} \right)^2 + \left( \frac{{}^i C_{\text{Cr,calc}}^{\text{interf}} - \bar{C}_{\text{Cr,exp}}^{\text{interf}}}{\bar{C}_{\text{Cr,exp}}^{\text{interf}}} \right)^2 + \left( \frac{D_{\text{Cr}}^i - \bar{D}_{\text{Cr}}}{\bar{D}_{\text{Cr}}} \right)^2 \right] \quad (2)$$

where  ${}^i C_{\text{Cr,exp}}$  and  ${}^i C_{\text{Cr,calc}}$  are the  $i$ th measured and calculated (fitted) Cr-concentration profiles, respectively;  $D_{\text{Cr}}^i$  is the fitted value of the Cr chemical-diffusion coefficient pertaining to the  $i$ th calculated Cr-depletion profile ( $\bar{D}_{\text{Cr}}$  is the average value of the Cr chemical-diffusion coefficient as obtained from all  $N$  fitted Cr-depletion profiles);  ${}^i C_{\text{Cr,calc}}^{\text{interf}}$  is the value of the interface concentration for the  $i$ th calculated Cr-depletion profile;  $\bar{C}_{\text{Cr,exp}}^{\text{interf}}$  (=13.2 wt%) represents the measured (average) steady-state-interface concentration during the parabolic-oxide-growth stage as determined by EPMA (see Fig. 8a).

Experimental and fitted Cr-depletion profiles can be compared in Fig. 10; a good agreement has been achieved. The resulting arithmetic mean values and their standard deviations for  $D_{\text{Cr}}^i$ ,  $k_{\text{Cr}_2\text{O}_3}^i$  and  ${}^i C_{\text{Cr}}^{\text{interf}}$  are  $\bar{D}_{\text{Cr}} = 1.49(\pm 0.05) \times 10^{-15} \text{ m}^2/\text{s}$ ,  $\bar{k}_{\text{Cr}_2\text{O}_3} = 1.33(\pm 0.06) \times 10^{-16} \text{ m}^2/\text{s}$  and  $\bar{C}_{\text{Cr}}^{\text{interf}} = 13.1(\pm 0.4) \text{ wt}\%$ , respectively. The value of  $\bar{D}_{\text{Cr}} = 1.49(\pm 0.05) \times 10^{-15} \text{ m}^2/\text{s}$  falls well within the range of values of  $5 \times 10^{-16}$  to  $1.3 \times 10^{-14} \text{ m}^2/\text{s}$ , comprising the diffusion coefficient data reported for Fe–27Cr–20Ni–1.5Si [34], and Fe–20Cr–25Ni–(Nb) [35], alloys at 1,286 K. The value of  $\bar{k}_{\text{Cr}_2\text{O}_3} = 1.33(\pm 0.06) \times 10^{-16} \text{ m}^2/\text{s}$  compares well with the experimental value of  $2.4(\pm 1.1) \times 10^{-16} \text{ m}^2/\text{s}$ , as determined independently for all oxidation times by cross-sectional SEM analysis in the present study (section “Morphology and Phase Constitution of the Grown Oxide Scale”).

Adopting the thus-determined values of  $\bar{D}_{\text{Cr}}$  and  $\bar{k}_{\text{Cr}_2\text{O}_3}$ , as well as  $C_{\text{Cr}}^{\text{centre}} < C_{\text{Cr}} = 16 \text{ wt}\%$  as the criterion for breakaway oxidation (see above), the

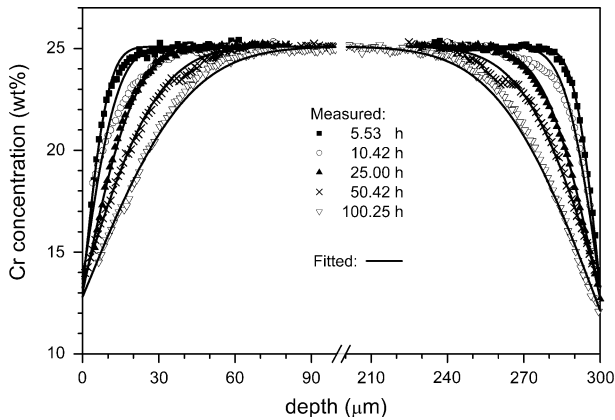


**Fig. 10** Measured (data points) and model-fitted (solid lines) concentration-depth profiles of Cr in the alloy substrate (300  $\mu\text{m}$ -thick) after oxidation at 1,286 K for various times in the range of 5.53–100.25 h. See section “Lifetime Prediction” for details

time to breakaway oxidation of the Fe–25Cr–20Ni–2.8Si sheet under isothermal-oxidation conditions at 1,286 K can be calculated as function of the sheet thickness. The result is shown in Fig. 11. It follows that the lifetime of a Fe–25Cr–20Ni–2.8Si alloy component of sheet-like geometry under isothermal oxidation at 1,286 K increases as the square of the sheet thickness from about 12 h to more than 2,600 h for an increase in sheet thickness from 20 to 300  $\mu\text{m}$ .

The model prediction has been verified in the present study by isothermal oxidation of a relatively thin sheet of Fe–25Cr–20Ni–2.8Si alloy, with a thickness of 140  $\mu\text{m}$ , beyond breakaway oxidation (i.e., for 552 h at 1,286 K in air; see sections “Morphology and Phase Constitution of the Grown Oxide Scale” and “Compositional Changes in the Alloy Substrate”). According to the model prediction, the 140  $\mu\text{m}$ -thick alloy sheet should have reached the breakaway oxidation stage in the oxidation time interval of 549–600 h (see Fig. 11).<sup>2</sup> Indeed, analysis of the 140  $\mu\text{m}$ -thick alloy sheet surface after 552 h of oxidation at 1,286 K indicates that the sample has entered the breakaway oxidation regime (sections “Morphology and Phase Constitution of the Grown Oxide Scale” and “Compositional Changes in the Alloy Substrate”). According to the model, the midsection and interface Cr concentrations in the alloy after 552 h of oxidation at 1,286 K in air should have dropped to values of about 16.2( $\pm 0.2$ ) wt% and 11.4( $\pm 0.3$ ) wt% (see footnote 2), respectively, which are higher than the corresponding experimentally determined values of 11.6( $\pm 1$ ) wt% and 8.9( $\pm 1$ ) wt%, respectively (see Fig. 9 and section “Compositional Changes in the Alloy Substrate”). The lower values for the experimentally determined Cr concentrations in the breakaway-oxidation stage can

<sup>2</sup> The indicated time interval for the calculated onset of the breakaway-oxidation time, as well as the indicated errors in the calculated Cr concentrations of the 140  $\mu\text{m}$ -thick alloy sheet after 552 h of oxidation, have been obtained by considering the errors in the arithmetic values of the parabolic-growth constant and the Cr-diffusion coefficient as obtained by the fitting of the model to the experimental Cr-depletion profiles.

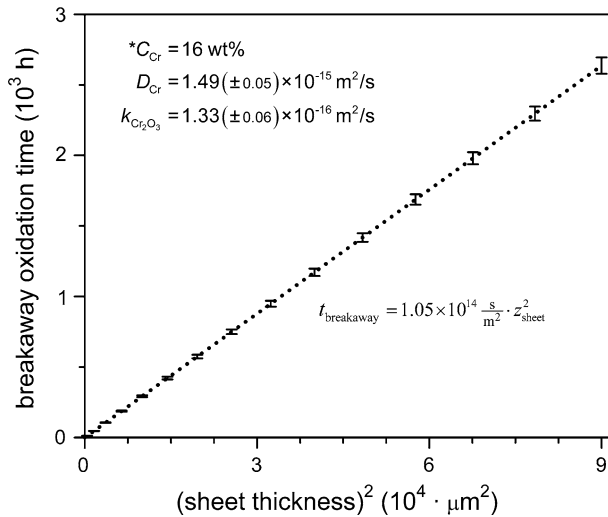


**Fig. 11** Predicted breakaway-oxidation time as a function of the alloy sheet thickness, as calculated for the isothermal oxidation of the Fe–25Cr–20Ni–2.8Si alloy at 1,286 K in air. The breakaway time was taken equal to the oxidation time after which the Cr concentration at the midplane of the sheet has dropped below the critical-healing concentration of 16 wt%. See section “Lifetime Prediction” for details. The error bars for the breakaway oxidation time have been obtained by considering the error in the values used of the parabolic-growth constant and the Cr-diffusion coefficient as obtained from the fitting to the experimental Cr-depletion profiles (see Fig. 9 and section “Lifetime Prediction”)

be attributed to extensive, additional Cr depletion by internal-nitride precipitation during the breakaway-oxidation stage (section “Compositional Changes in the Alloy Substrate”), which is not accounted for in the model calculations.

## Conclusions

Upon isothermal oxidation of a chromia-forming Fe–25Cr–20Ni–2.8Si austenitic steel at 1,286 K in air, initially a double-layered oxide structure develops, which consist of a *bottom* layer of amorphous  $\text{SiO}_2$  adjacent to the alloy/oxide interface and a *top* layer of  $\text{Cr}_2\text{O}_3$  adjacent to the surface containing some mixed (Ni,Cr,Fe)-oxides and/or  $\text{NiCr}_2\text{O}_4$  spinel oxides at the outer oxide surface. Parabolic-oxide-growth kinetics were found to prevail after 5–10 h of oxidation with a corresponding steady-state-Cr concentration in the alloy at the alloy/oxide interface of about  $13(\pm 1)$  wt%. Extensive cracking and/or spallation of the oxide scale (predominantly along the alloy/ $\text{SiO}_2$  scale interface and in association with the formation of  $\text{Cr}_2\text{N}$  precipitates and internal oxidation of Si and Cr in the less-depleted regions in the interior of the alloy substrate) not only takes place upon cooling, but also during isothermal oxidation at 1,286 K already before breakaway oxidation. Breakaway oxidation eventually occurs, when the ‘bulk’-Cr concentration in the interior of the alloy falls below the critical value required to ‘heal’ the protective-oxide layer after oxide spallation.

Adopting parabolic growth of the oxide and volume diffusion of Cr in the substrate as parameters in a model to describe the oxidation kinetics and associated compositional changes in the parent alloy, values of  $D_{Cr} = 1.49(\pm 0.05) \times 10^{-15} \text{ m}^2/\text{s}$  and  $k_{Cr_2O_3} = 1.33(\pm 0.06) \times 10^{-16} \text{ m}^2/\text{s}$  could be determined by simultaneous fitting to a series of Cr-concentration-depth profiles in the parent alloy substrate determined experimentally after various oxidation times at 1,286 K within the parabolic-growth regime. On this basis, a lifetime prediction (i.e., time until the start of the breakaway-oxidation regime) of Cr-containing, austenitic-steel sheets subjected to oxidation can be made. This model for lifetime calculation provides predictions which agree with experimental results and can therefore serve as an efficacious tool for component dimensioning in high-temperature applications of this class of steels.

**Acknowledgements** The authors are indebted to Dipl.-Ing. B. Siegle for the AES analysis, Dipl.-Ing. G. Maier for XRD analysis and S. Haug for the EPMA measurements. We gratefully acknowledge the involvement of Dr. A. Mattern for scientific support and advice (Robert Bosch GmbH).

**Open Access** This article is distributed under the terms of the Creative Commons Attribution Non-commercial License which permits any noncommercial use, distribution, and reproduction in any medium, provided the original author(s) and source are credited.

## References

1. R. C. Lobb and H. E. Evans, *Corrosion Science* **23**(1), 55 (1983).
2. R. C. Lobb and H. E. Evans, *Corrosion Science* **24**(5), 385 (1984).
3. H. E. Evans, D. A. Hilton, R. A. Holm et al., *Oxidation of Metals* **14**(3), 235 (1980).
4. H. E. Evans, D. A. Hilton, and R. A. Holm, *Oxidation of Metals* **10**(3), 149 (1976).
5. H. E. Evans, D. A. Hilton, R. A. Holm et al., *Oxidation of Metals* **12**(6), 473 (1978).
6. D. G. Lees and J. M. Calvert, *Corrosion Science* **16**(10), 767 (1976).
7. T. J. Nijdam, L. P. H. Jeurgens, and W. G. Sloof, *Acta Materialia* **51**(18), 5295 (2003).
8. B. D. Bastow, D. P. Whittle, and G. C. Wood, *Oxidation of Metals* **12**(5), 413 (1978).
9. H. E. Evans, A. T. Donaldson, and T. C. Gilmour, *Oxidation of Metals* **52**(5–6), 379 (1999).
10. H. E. Evans and A. T. Donaldson, *Oxidation of Metals* **50**(5–6), 457 (1998).
11. D. P. Whittle, *Oxidation of Metals* **4**(3), 171 (1972).
12. D. J. Baxter, R. C. Hurst, and R. T. Derricott, *Materials and Corrosion* **35**(6), 266 (1984).
13. H. E. Evans, D. A. Hilton, R. A. Holm et al., *Oxidation of Metals* **19**(1–2), 1 (1983).
14. B. Gleeson and M. A. Harper, *Oxidation of Metals* **49**(3–4), 373 (1998).
15. F. H. Stott, G. C. Wood, and J. Stringer, *Oxidation of Metals* **44**(1–2), 113 (1995).
16. D. J. Baxter, R. T. Derricott, and R. C. Hurst, *Materials and Corrosion* **34**(9), 446 (1983).
17. D. L. Douglass and J. S. Armijo, *Oxidation of Metals* **2**(2), 207 (1970).
18. A. Kumar and D. L. Douglass, *Oxidation of Metals* **10**(1), 1 (1976).
19. M. Baccalaro, A. Mattern, I. Hauer, et al., in *Proceedings Euro PM2005*, edited by (EPMA, 2005), p. 395.
20. S. N. Basu and G. J. Yurek, *Oxidation of Metals* **36**(3–4), 281 (1991).
21. R. C. Lobb, J. A. Sasse, and H. E. Evans, *Materials Science and Technology* **5**(8), 828 (1989).
22. F. H. Stott, G. J. Gabriel, F. I. Wei et al., *Materials and Corrosion* **38**(9), 521 (1987).
23. D. P. Whittle, *Corrosion Science* **12**(11), 869 (1972).
24. International Centre of Diffraction Data, Newton Square, PA, USA (1997–2007).
25. J.L. Pouchou and F. Pichoir, *Recherche Aerospatiale* (3), 167 (1984).
26. T. J. Nijdam, L. P. H. Jeurgens, J. H. Chen et al., *Oxidation of Metals* **64**(5–6), 355 (2005).
27. J. M. Francis and J. A. Jutson, *Materials Science and Engineering* **4**(2–3), 84 (1969).

28. H. E. Evans, in *Cyclic Oxidation of High Temperature Materials*, Eds. M. M. Schütze, W. J. Quaddackers (Institute of Materials, London, 1999), p. 3.
29. J. Erneman, M. Schwind, P. Liu et al., *Acta Materialia* **52**(14), 4337 (2004).
30. B. E. Deal and A. S. Grove, *Journal of Applied Physics* **36**(12), 3770 (1965).
31. W. G. Sloof and L. P. H. Jeurgens, *Microchimica Acta* **145**(1–4), 215 (2004).
32. G. Y. Lai, *High-temperature Corrosion of Engineering Alloys*. (ASM International, Materials Park, Ohio, 1990).
33. Matlab, 7.1.0.246 (R14) Service Pack 3, Natick (2005).
34. A. F. Smith and G. B. Gibbs, *Metal Science Journal* **3**, 9 (1969).
35. P. I. Williams and R. G. Faulkner, *Journal of Materials Science* **22**(10), 3537 (1987).